Analyst

LA-ICP-MS and MALDI-MS image registration for correlating nanomaterial biodistributions and their biochemical effects

Journal:	*Analyst*
Manuscript ID	AN-ART-09-2021-001783.R1
Article Type:	Paper
Date Submitted by the Author:	12-Nov-2021
Complete List of Authors:	Castellanos-García, Laura; University of Massachusetts Amherst, Chemistry Sikora, Kristen; University of Massachusetts Amherst, Department of Chemistry Doungchawee, Jeerapat; University of Massachusetts Amherst, Chemistry Vachet, Richard; University of Massachusetts, Department of Chemistry

SCHOLARONE™
Manuscripts

LA-ICP-MS and MALDI-MS image registration for correlating nanomaterial biodistributions and their biochemical effects

Laura J. Castellanos-Garcia, Kristen N. Sikora, Jeerapat Doungchawee, and Richard W. Vachet*

Department of Chemistry, University of Massachusetts Amherst

*Corresponding author:
240 Thatcher Way
Life Sciences Laboratory, N363
University of Massachusetts Amherst
Amherst, MA 01003
rwvachet@chem.umass.edu

Abstract

Laser ablation inductively-coupled plasma mass spectrometry (LA-ICP-MS) imaging and matrix assisted laser desorption ionization mass spectrometry imaging (MALDI-MSI) are complementary methods that measure distributions of elements and biomolecules in tissue sections. Quantitative correlations of the information provided by these two imaging modalities requires that the datasets be registered in the same coordinate system, allowing for pixel-by-pixel comparisons. We describe here a computational workflow written in Python that accomplishes this registration, even for adjacent tissue sections, with accuracies within ± 50 μm. The value of this registration process is demonstrated by correlating images of tissue sections from mice injected with gold nanomaterial drug delivery systems. Quantitative correlations of the nanomaterial delivery vehicle, as detected by LA-ICP-MS imaging, with biochemical changes, as detected by MALDI-MSI, provide deeper insight into how nanomaterial delivery systems influence lipid biochemistry in tissues. Moreover, the registration process allows the more precise images associated with LA-ICP-MS imaging to be leveraged to achieve improved segmentation in MALDI-MS images, resulting in the identification of lipids that are most associated with different sub-organ regions in tissues.

Introduction

Mass spectrometry imaging (MSI) comprises several techniques that allow the analysis of hundreds of molecules simultaneously, sometimes with spatial resolutions as low as 1 μm.[1,2] Among MSI techniques, matrix-assisted laser desorption/ionization (MALDI)[3–6] and desorption electrospray ionization (DESI)[7,8] have been extensively used for the spatially resolved analysis of metabolites,[9,10] lipids,[11,12] peptides,[13,14] proteins,[15,16] and exogenous analytes, like drugs.[17–19] In comparison, laser ablation inductively-coupled plasma MS (LA-ICP-MS) imaging can provide quantitative distributions of a wide range of elements within a sample.[20–22] Despite the near universal detection capabilities of MS, it is difficult to detect all compounds of interest in a given MSI experiment.[23,24] Furthermore, the right combination of MSI modalities can provide complementary information, allowing optimal information to be obtained from a given sample.[25–27] Properly combining the data from different imaging modalities can allow the strengths of each modality to be leveraged so that more in-depth information about a sample can be obtained.[28–31] For example, MALDI-MSI provides valuable biomolecule information but can suffer significant pixel-to-pixel signal variability.[32] On the other hand, LA-ICP-MS imaging is less subject to signal suppression and signal variability because samples are completely ablated, allowing it to provide quantitative information about metal distributions.[20] However, LA-ICP-MS imaging provides no molecular information due to its destructive nature.[21]

By appropriately leveraging the datasets from MALDI-MS and LA-ICP-MS imaging of a given tissue section, more precise and informative images should be accessible. The comparison of results from LA-ICP-MS and MALDI-MS imaging is usually done by visually overlaying the images generated by the techniques.[33–35] However, simple image overlays hinder quantitative correlations because the images have different coordinate systems and orientations. More sophisticated multimodal registration methods allow pixel-to-pixel analysis of tissue sections by transforming the coordinates of one modality into the other modality, which allows statistical comparisons (e.g. Pearson's correlations).[24] Such approaches have been used by Caprioli and co-workers to register MALDI MSI images with microscopy images[36] and Van Malderen et al. to register LA-ICP-MS and microcomputed tomography images,[37] although these approaches have not been used for LA-ICP-MS and MALDI-MS image registration. Holzlechner et al. recently reported an approach to align LA-ICP-MS and MALDI-MS images[38] that was based upon a multisensor image integration method that uses fiducial markers to arrange images in the same coordinate system.[39] Since the approach is based on fiducial markers, the accuracy of the registration is limited and only linear transformations of the images are possible, making it unsuitable for registering images from adjacent tissue slices.[36] Moreover, this alignment approach is performed in the software package Epina Imagelab[39], which is not open source or freely available.

Here, we describe a freely available computational workflow written in Python that allows the registration of LA-ICP-MS and MALDI-MS images in the same coordinate system, even for images from adjacent tissue sections, with accuracies within ± 50 μm. We illustrate the value of this registration approach by quantitatively correlating the distributions of nanomaterials with their biochemical effects. In addition, we demonstrate that the more precise imaging data from LA-ICP-MS imaging can be used to improve image segmentation in MALDI-MS images.

Materials and Methods

Nanomaterial Synthesis

Nanoparticle (NP) synthesis was performed using the Brust-Schiffrin reaction,[40] followed by functionalization of the AuNP core with surface ligands, as described in previous work.[41–44] Similarly, NP-stabilized capsules (NPSC) were synthesized by mixing arginine-coated NPs with linoleic acid, followed by its functionalization with siRNA that causes knockdown of tumor necrosis factor α (TNFα), as described in detail in previous reports.[45–47] The methods used to synthesize and characterize these nanomaterials are described in the supporting information (SI), along with the results from these characterization measurements.

Animal Experiments and Tissue Sectioning

Balb/c mice were tail-vein injected with the NPs or NPSCs and euthanized after 48 h. Mice were sacrificed by carbon dioxide inhalation and cervical dislocation. All animal experiments were approved by the University of Massachusetts Amherst Institutional Animal Care and Use Committee (IACUC), which is guided by the U.S. Animal Welfare Act and U.S. Public Health Service Policy. Tissues were flash frozen and kept at -80 °C until sectioned for imaging. Frozen tissues were sectioned using a LEICA CMM1850 cryostat. Adjacent tissue sections of 12 μm thickness were thaw-mounted on indium tin oxide (ITO)-coated glass for MALDI-MSI and glass slides for LA-ICP-MS imaging experiments.

MALDI-MSI

MALDI-MSI experiments were performed using 2,5-dihydroxybenzoic acid (2,5-DHB) as a matrix. Two different methods for matrix deposition were used: spraying and sublimation. Spraying was performed using a Bruker ImagePrep device to spray a 25 mg/mL matrix solution in 1:1 methanol:water on the sectioned tissue. Sublimation was performed on a home-built sublimation apparatus similar to the setup described by Chaurand and co-workers.[48] For liver tissue sections, 200 mg of matrix were deposited at 140 °C at 7 mTorr for 9 minutes. For spleen tissue sections, 170 mg of matrix were deposited at 140 °C at 7 mTorr for 8 minutes. Data acquisition was performed on a Bruker UltrafleXetreme MALDI TOF/TOF at 50 μm resolution over a *m/z* range of 200 to 2000. MS/MS experiments to confirm analyte identities were performed in a collision-induced dissociation (CID) LIFT cell.

LA-ICP-MS imaging

LA-ICP-MS images of ^{197}Au, ^{57}Fe, and ^{66}Zn were acquired on a CETAC LSX-213 G2 laser ablation system coupled with a Perkin Elmer NexION 300x ICP-MS instrument. The following laser parameters were used: 50 μm spot size, 20 μm/s scan rate, 3.65 J laser energy, 10 Hz laser frequency, and a 10 s shutter delay. The helium carrier gas from the laser ablation system was set to 0.6 L/min. Other ICP-MS experimental parameters were similar to those used in previous reports on the LA-ICP-MS analysis of nanomaterials in tissue sections.[49–51]

Image preprocessing

MALDI-MS images were normalized and exported as imzML files using FlexImaging (Bruker, Daltonics). The imzML files were imported to Python using the pyimzML parser, developed previously.[52] Peak picking was performed using SCiLS Lab 2015b, and the list of selected ions and mass tolerances were imported to Python as a text file. Images of the selected ions were rendered with the pyimzML parser. LA-ICP-MS images were reconstructed, analyzed, and segmented using a custom Python script RecSegImage-LA, which was described recently and is freely available at GitHub (https://github.com/Vachet-Lab/RecSegImage-LA).[53] Hotspot removal was performed on MALDI-MS and LA-ICP-MS images by selecting the intensities in the >0.99 quantile and replacing them with the 0.99 quantile value.[54] In some cases, t-stochastic non-linear embedding (t-SNE) dimensionality reduction module from the scikit-learn Python library[55] was applied to selected ion images in MALDI-MSI data to obtain a single image representation of the dataset.

Image registration and validation

Image registration was performed using the SimpleElastix[56] Python extension of the Elastix C++ library.[57] The MALDI-MSI image (t-SNE or heme channel) was set as the fixed image, while the LA-ICP-MS image (Fe channel) was set as the moving image. Registration was performed using the default affine parameter map followed by the default non-linear parameter map in SimpleElastix with certain modifications as follows: 4,000 iterations for the affine parameter map, 8,000 iterations for the non-linear parameter map and 50 final grid spacing in physical units. Validation of the registration was performed using Dice similarity coefficient calculations (DSC), as described by Klein and co-workers (equation 1), where X and Y represent the binary label images. Selected regions, such as veins in the liver and white pulp spleen regions in the spleen, were manually selected in Fiji,[58] and imported to Python to calculate the DSC value. Landmark distance analysis after registration was calculated by selecting corresponding points in the two images, followed by image overlay and calculation of their distances in Fiji.

$$DSC(X,Y) = \frac{2|X \cap Y|}{|X| + |Y|}$$ **equation 1**

Statistical analysis of the registered images

Correlation coefficients between ionic signals in MALDI-MSI and LA-ICP-MS imaging data were calculated using the implementation of Pearson correlations in the Scipy library[59] on the vectorized, background subtracted MALDI-MS and LA-ICP-MS images.

Results

Registration of LA-ICP-MS and MALDI-MS images

Image registration involves transforming two or more images containing different data features into the same coordinate system. Once the images are registered, the combined information from the different imaging modalities allows deeper statistical and quantitative analyses of the images. In the process of image registration, one of the images is set as the fixed image, and the other one is the moving image (e.g., Figure S1). The moving image is transformed to maximize its similarity to the fixed image, resulting in an image that has the same coordinates and pixel number as the fixed image. In this work, LA-ICP-MS and MALDI-MS images were registered using SimpleElastix registration algorithms[56] in a custom Python workflow. Access to the scripts, examples and documentation can be found at GitHub: https://github.com/Vachet-Lab/MS-Registration.

Our approach to registration of LA-ICP-MS and MALDI-MS images relies on the use of internal signal features to drive the optimization process, as it seeks to maximize the mutual information present in both images. Ideally, these signal features should reflect the morphologic structure of the image (e.g., distinct sub-organ regions in a tissue) to ensure the best registration possible. Proper choice of the signal channels enables successful registration of LA-ICP-MS and

MALDI-MS images when different MALDI matrix deposition approaches are used or even when adjacent tissue sections are imaged. For LA-ICP-MS, we find that the Fe signal channel (i.e., ^{57}Fe) is an effective feature to use as it indicates blood-rich regions that often define different regions in a tissue. For MALDI-MS images, we initially used the heme signal (*m/z* 616), as analogous indicator of blood flow. Figures 1a and b illustrate the LA-ICP-MS (red) and MALDI-MS (blue) images of liver and spleen tissue sections before and after registration. The MALDI-MS image was used as the fixed image, and the LA-ICP-MS image was used as the moving image. Visual inspection of these images shows that the registration process successfully aligns the tissue boundaries and other internal structure features. For example, in Figure 1a, a large piece of connective tissue (CT) that is devoid of heme signal in the MALDI image aligns well with the same low Fe signal in the LA-ICP-MS image. Similarly, the red pulp (RP) and white pulp (WP) regions of the spleen are very well aligned after registration (Figure 1b).

Registration of LA-ICP-MS and MALDI-MS images can also be accomplished when the matrix in MALDI-MS is deposited via sublimation. After matrix sublimation, we find that the heme signal is less reliably abundant, so we used a dimensionality reduction strategy, which leverages the many more signal channels that are present in MALDI-MSI datasets, to generate the signal features for the registration process. Dimensionality reduction was accomplished using a t-distributed stochastic neighbor embedding (t-SNE) approach that has been used successfully on MALDI-MSI data.[60–62] Using liver tissue sections as an example, t-SNE can be used effectively to combine nearly 40 different ions measured in MALDI-MS images (Figure S2). When the t-SNE generated features from MALDI-MS images are used together with the Fe signal from LA-ICP-MS, registration of the two images can be achieved. Our approach successfully registers the two images (Figure 1c), as indicated by the excellent overlap of the tissue boundaries and veins (V) in the images. It should be noted that the registered images shown in Figure 1 are from adjacent tissue sections. Using adjacent tissue slices allows MALDI-MS and LA-ICP-MS imaging conditions to be separately optimized. Registering adjacent tissue sections is only possible using non-linear registration approaches (Figure S3) to correct for local deformations in the tissues that can arise from placement of adjacent tissue slices.

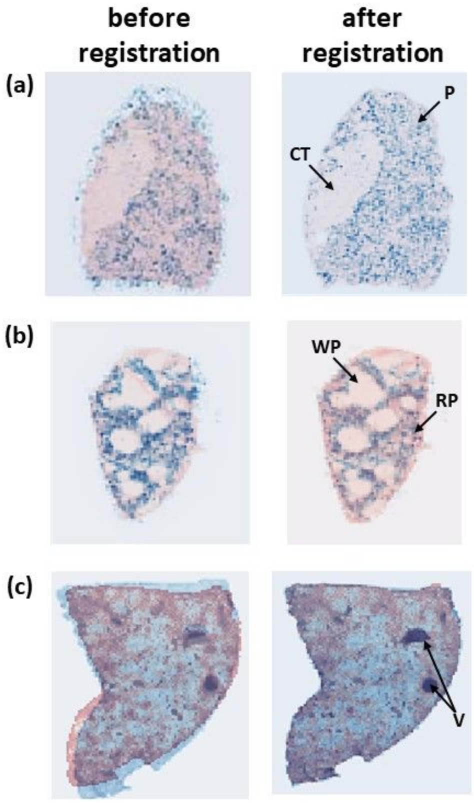

Figure 1. Sequential slices of liver and spleen tissues from mice analyzed by LA-ICP-MS (red) and MALDI-MS (blue) using different MALDI-MS matrix deposition strategies and compared before and after registration. (a) Liver: The MALDI-MS tissue sample was prepared using a matrix sprayer. Low heme and Fe signals are present in the connective tissue (CT), while higher heme and Fe signals are present in the parenchyma (P). (b) Spleen: The MALDI-MS tissue sample was prepared using a matrix sprayer. High Fe and heme signals are present in the red pulp (RP), while low signals are found in the white pulp (WP). (c) Liver: The MALDI-MS tissue sample was prepared using a sublimation chamber. High Fe and t-SNE signals are present in the vein (V).

Registration evaluation

The effectiveness of our registration approach was evaluated by two methods: Dice similarity coefficient (DSC) calculations and landmark validation. DSC values were calculated using the approach described by Rohlfin[63] (equation 1). For calculating the DSC values, regions of interest (ROI) were first chosen in both the LA-ICP-MS and MALDI-MS images (Figure 2). The chosen ROIs depended on the tissue type. For the liver, we used blood vessels, and for the spleen, we used the white pulp. Figure 2 shows the DSC analysis for the chosen ROIs. White pixels in the overlay represent pixels that overlap in LA-ICP-MS and MALDI-MS images. The DSC value for the liver images increases from 0.42 after simple translation of the images to 0.85 after full registration of the images, and in the spleen tissue the increase is from 0.64 to 0.77. Perfect overlap of the images would correspond to DSC values of 1.0. Because these images are from adjacent tissue slices, DSC values below 1.0 are expected, as there are slight differences in the

ROIs due to biological variations and imperfect placement of the tissue sections. The improvement in DSC values after registration is comparable to what was achieved using analogous approaches when MALDI-MS and immunostained images of liver and spleen sections were registered.[64] To further test the ability of our registration methods, we also tested tissues sections that were not immediately adjacent but were two sections apart. In one example, the DSC value increased from 0.34 to 0.69 after registration (Figure S4), indicating there is reasonable similarity between non-adjacent tissue sections.

Landmark validation[36] was also used to assess registration effectiveness. In the landmark approach, several morphologically distinct points are chosen in both LA-ICP-MS and MALDI-MS images, and the distance between these points is calculated and averaged to provide an effective registration accuracy (Figure S5). For the images shown in Figure 2, average registration accuracies of 40 ± 30 μm and 70 ± 20 μm are obtained for the liver and spleen, respectively. Since the images were acquired at 50 μm resolution, the landmark distances show that most of the pixels are either perfectly correlated or are one pixel off. Given that the diameters of veins in the liver vary between 300 and 600 μm, and the diameters of white pulp areas are typically between 300 and 900 μm, these registration accuracies allow us to make confident conclusions about the veins and white pulp sub-organ regions.

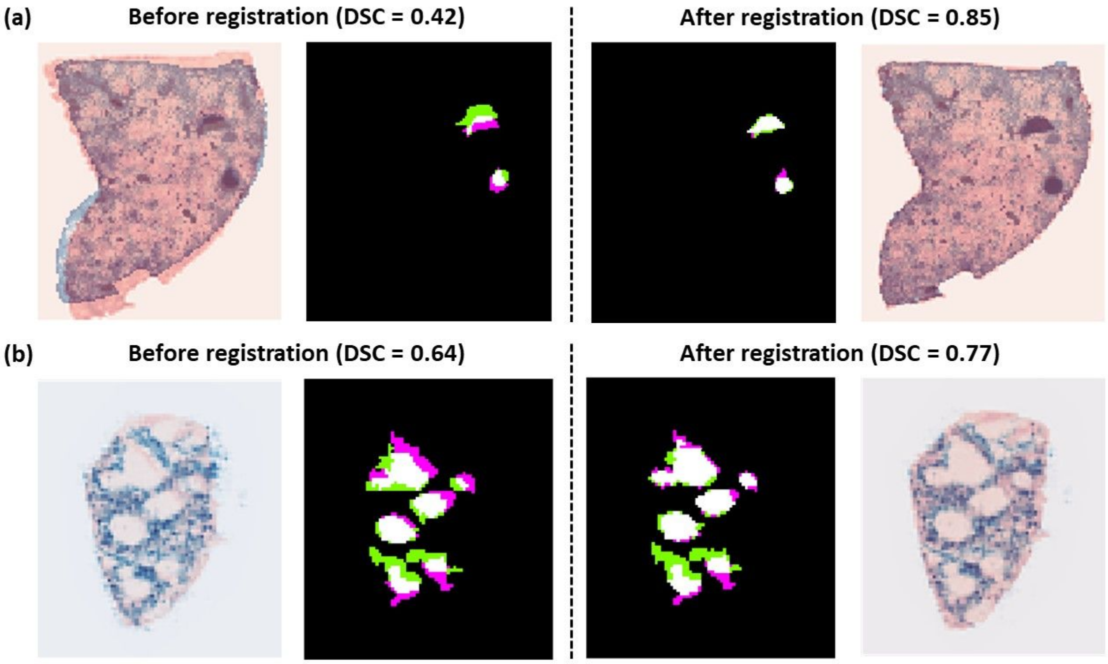

Figure 2. Registration validation using DSC calculations for liver and spleen tissue sections after registration of the MALDI-MS and LA-ICP-MS images from figures 1b and c. (a) Overlay of blood vessel masks and resulting DSC values before and after registration. (b) Overlay of white pulp masks and resulting

DSC values before and after registration. Green = LA-ICP-MS only pixels, Magenta = MALDI-MS only pixels, White = overlaid pixels. Segmentation of the veins and white pulp was performed manually using the Fe image in LA-ICP-MS and the t-SNE image in MALDI-MS to generate computational masks for each of the two images.

Statistical correlations between chemical information in both images

Once the images are registered, we can then compare how the signals in one image modality correlate with the signals in the other modality, which allows us to understand better the underlying biochemistry of the tissues. Using Pearson's correlations, which are one of the more accurate methods for quantifying the degree of co-localization in two images,[54] we can compare the extent to which metal distributions that are detected in LA-ICP-MS images correlate to specific biomolecule distributions that are detected in MALDI-MS images (Figure S6). As examples, we correlate Fe signals in LA-ICP-MS images of the liver and spleen with a range of lipids that are observed in MALDI-MS images of these same organs (Figure 3a and 3c). For the spleen, we find that the signal levels for two classes of lipids, including ceramides (Cer) and some phosphatidylethanolamines (PE), correlate with the Fe signals as these lipids are expected to be present in the red pulp.[65] Since high Fe signals in LA-ICP-MS indicate the location of red pulp regions in the spleen, the lipids that positively correlate with the Fe are predominantly located in the red pulp. In contrast, the lipids that anticorrelate with the Fe, including lysophosphatidylcholines (LPC), phosphatidylcholines (PC), sphingomyelins (SM),[65] and carnitines (Car), are predominantly located in the white pulp, which has low Fe levels. In effect, we have identified several lipids that can act as biomarkers of the red and white pulp regions of the spleen.

The value of these correlations is even more evident when we image tissue sections from mice injected with gold nanomaterial delivery agents such as NPSCs that deliver TNFα-specific siRNA (Figure S7). These NPSCs have shown the ability to knockdown the production of TNFα in cell culture and in animals,[45–47] and this knockdown causes changes in the levels of various lipids.[66] LA-ICP-MS imaging is capable of indicating the distributions of the Au from the nanomaterials, while MALDI-MS images can indicate how biomolecules change in response to knockdown of TNFα. We correlated the Fe and Au signals with the lipids for control and NPSC-treated mice in both liver and spleen tissue sections (Figure 3), which are the organs that have the highest concentrations of Au. Several of the lipids exhibit a significant change in their Pearson correlation values in spleens taken from NPSC-treated mice as compared to control mice (Figure 3a). For example, glucoceramide (Glc) d18:1/16:1(17Z) has a low correlation coefficient with Fe (i.e., 0.03) in the control tissue, which indicates the signal is located equally in the Fe-rich red pulp region and the Fe-poor white pulp region. After NPSC treatment, the Glc d18:1/16:1(17Z) correlation with Fe increases to 0.32, indicating greater levels of this lipid in the red pulp. Because the Au signal also highly correlates with this lipid (Figure 3b) and the Fe and Au signals have a high positive correlation value of 0.69 (see Figure S8), we conclude that the presence of the NPSC promotes changes in the Glc d18:1/16:1(17Z) levels. Glucosylceramides are known markers of inflammation,[67] so it is possible that the presence of the NPSCs causes localized inflammation in the red pulp where they accumulate. PC (34:1) exhibits a similar behavior with its Pearson's value changing from -0.09 in the control to 0.14 in the NPSC-treated tissue. This lipid also positively correlates with Au, suggesting an NPSC-induced effect to the level of this lipid as well.

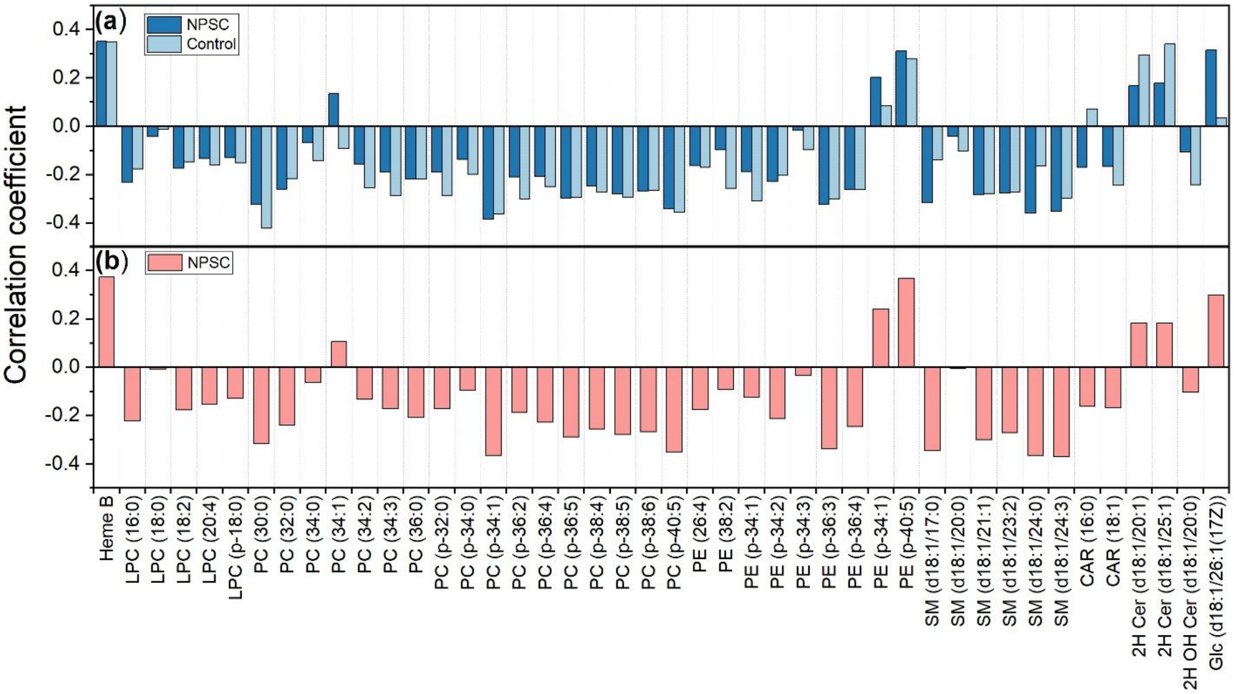

Figure 3. Pearson's correlation coefficients obtained after registering LA-ICP-MS and MALDI-MS images of spleen tissue sections from control and NPSC treated mice (MS images are found in Figure S9). (a) Correlation coefficients for Fe and select lipids that are measured from control and NPSC-treated mice. (b) Correlation coefficients for Au and select lipids that are measured from NPSC-treated mice. LPC = lysophosphatidylcholines; PC = phosphatidylcholines; PE = phosphatidylethanolamines; SM = sphingomyelins; CAR = carnitines; Cer = ceramides; Glc = glucosylceramides.

In contrast, many more lipids show the opposite trend, becoming more negatively correlated with Fe and Au. For example, CAR (16:0) and SM (d18:1/17:0) have correlation values that change from 0.07 and -0.14 to -0.17 and -0.32, respectively. These anti-correlated values suggest that the presence of the NPSCs is generating changes to the levels of these lipids in places where the Fe and Au concentrations are low. That means that these lipid changes are occurring primarily in the white pulp where Fe concentrations are low and where Au accumulation is minimal (Figure S8). TNFα knockdown therapies, like these NPSCs, typically target macrophages and lymphocytes, which are highly abundant in the white pulp of the spleen,[68] likely explaining why so many lipid changes occur in the white pulp. CAR (16:0), SM (d18:1/17:0), and several of the PC lipids are signaling lipids known to undergo changes in concentrations upon TNFα suppression,[66] and the ability to correlate MALDI-MS and LA-ICP-MS images helps identify the specific sub-organ regions in which these changes are happening.

LA-ICP-MS assisted segmentation of MALDI-MS images

The analysis of tissue regions upon MSI often involves the division of the image into segments so that the detected molecular features can be associated with different cell types and regions of the analyzed tissue. A commonly used methods for such image segmentation is k-means clustering, which is a statistical method that divides the image into segments that possess similar spectral characteristics, while being agnostic to the spatial structure of the data.[69] In MALDI-MS imaging, several approaches have been used to further improve segmentation, such as the implementation of more sophisticated spatially aware methods[70,71] and spatially-shrunken centroids.[72] Although segmentation algorithms for MALDI-MS imaging analysis are well developed, they highly depend on data quality, making the segmentation process challenging for noisy datasets.[72] LA-ICP-MS imaging usually produces less noisy images than MALDI-MSI primarily because the tissue section is completely ablated during the imaging process. Consequently, we sought to leverage this higher precision in LA-ICP-MS imaging to improve segmentation in MALDI-MS images. To do this, we first segment the LA-ICP-MS image and then apply the resulting segmentation masks to the registered MALDI-MS images to improve the segmentation of the MALDI-MS data.

As an example of LA-ICP-MS-assisted segmentation of MALDI-MS images, imaging data from mouse spleen tissues were acquired by both techniques (Figures 4a and b). First, we segmented the MALDI-MS images using two methods available in SCiLS lab: (i) k-means on the normalized dataset with a cluster number of 4 (Figure 4c) and (ii) bisecting k-means (Figure 4d). Both segmentation approaches differentiate the red and white pulp regions of the spleen, but neither method identifies a segment associated with the marginal zone, which is the ~100 μm-sized region where initial immune responses occur in this organ.[73] In contrast, segmentation of the Fe image from LA-ICP-MS imaging using RecSegImage-LA[53] does classify the marginal zone of the spleen as a separate segment in the image in addition to the red and white pulp regions (Figure 4e). The three segmented areas from the LA-ICP-MS image can then be used as computational masks to classify the lipid signals from the MALDI-MS images that are most associated with each of the three different regions of the spleen (Figure 4f, g, and h). This lipid classification is accomplished by separately averaging the lipid ion signals from the pixels associated with each of the three separate regions. Statistical t-tests were then used to identify lipids that had significant differences between regions in the spleen (Table 1). From these analyses, several lipids have significant differences in ion signals in the red pulp, white pulp, and marginal zone regions of the spleen. As examples, Figure 5 shows the MALDI-MS images of PE (p-40:5), which localizes well in the red pulp, PC (p-40:5), which localizes in the white pulp, and SM (d18:1/20:0), which is somewhat enriched in the marginal zone.

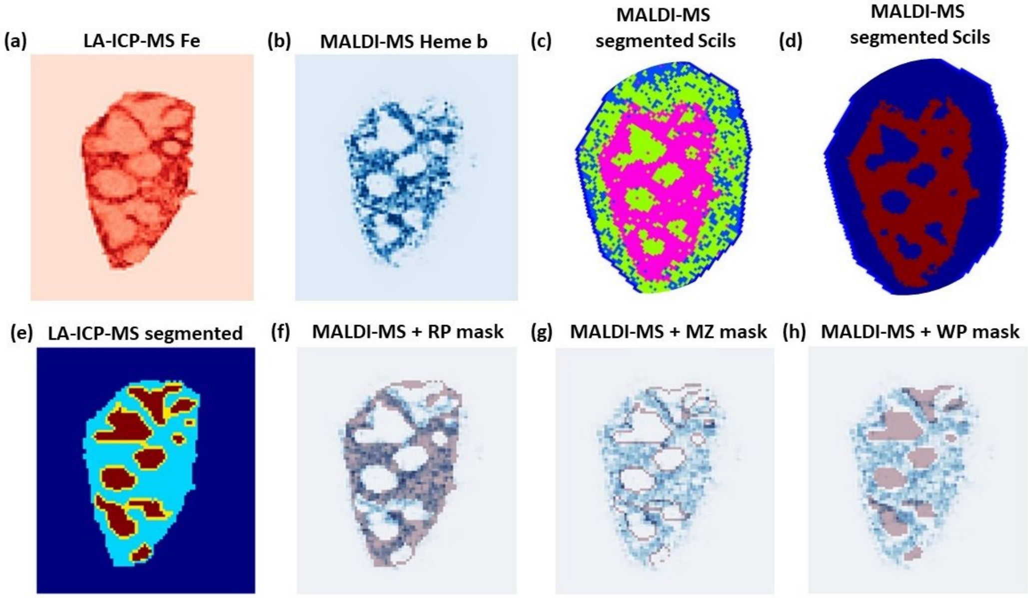

Figure 4. LA-ICP-MS assisted segmentation of MALDI-MS images. (a) LA-ICP-MS Fe image. (b) MALDI heme b image. (c) MALDI segmentation in SCiLS using k-means with a cluster number of 4. (d) MALDI segmentation in SciLS using bisecting k-means. (e) LA-ICP-MS segmentation using RecSegImage-LA,[53] and MALDI heme b images overlaid with the (f) red pulp (RP) mask, (g) marginal zone (MZ) mask, and (h) white pulp (WP) mask.

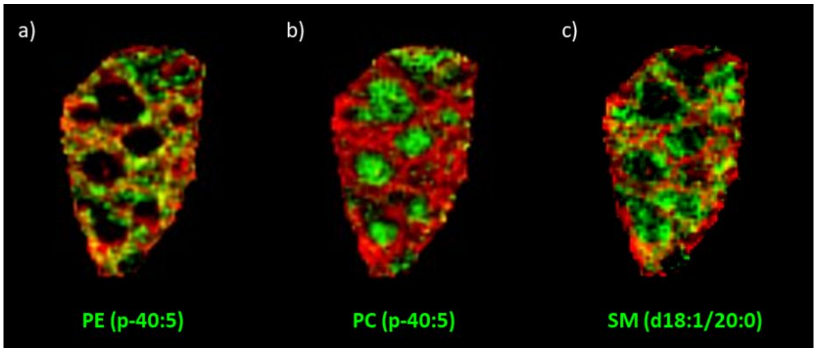

Figure 5. Correlation of Au vs lipids located on: (a) Red Pulp PE (p-40:5), (b) white pulp PC (p-40:5) and (c) marginal zone SM (d18:1/20:0).

Table 1. Normalized average signal intensities and standard deviations (SD) in each of the segmented regions (red pulp, white pulp, and marginal zone) of LA-ICP-MS and MALDI-MS ion signals, and determinations of unique localizations of each measured compound.

Ion identity	Red Pulp		White Pulp		Marginal Zone		t test probabilities (P)[a]		
	Average	SD	Average	SD	Average	SD	RP vs WP	RP vs MZ	WP vs MZ
Au	60.5	19.1	19.2	6.5	34.3	12.3	Yes	Yes	Yes
Fe	71.9	14.8	44.6	3.2	50.1	7.0	Yes	Yes	Yes
Heme B	53.3	25.9	24.9	21.5	39.3	26.1	Yes	Yes	Yes
LPC (16:0)	52.8	11.2	60.6	13.5	57.1	13.2	Yes	Yes	Yes
LPC (18:0)	37.1	13.9	36.7	11.9	38.9	13.6	No	No	No
LPC (18:2)	72.0	6.6	75.0	6.8	74.1	6.6	Yes	Yes	No
LPC (20:4)	46.2	13.9	52.2	14.4	48.8	13.6	Yes	No	Yes
LPC (p-18:0)	43.9	14.4	50.3	15.9	47.8	16.3	Yes	Yes	No
PC (30:0)	44.8	8.9	54.8	11.9	49.9	10.4	Yes	Yes	Yes
PC (32:0)	49.0	20.6	63.9	23.7	61.5	25.5	Yes	Yes	No
PC (34:0)	46.3	14.1	47.6	13.7	48.5	12.8	No	No	No
PC (34:1)	51.7	16.7	44.7	13.4	49.5	15.4	Yes	No	Yes
PC (34:2)	59.2	15.9	62.8	15.6	66.6	17.9	Yes	Yes	No
PC (34:3)	50.6	14.2	56.0	15.0	58.0	17.9	Yes	Yes	No
PC (36:0)	54.5	16.6	64.4	19.8	62.7	18.9	Yes	Yes	No
PC (p-32:0)	50.6	14.2	56.0	15.0	58.0	17.9	Yes	Yes	No
PC (p-34:0)	47.9	18.7	51.6	20.5	55.9	20.1	Yes	Yes	No
PC (p-34:1)	55.8	13.8	74.3	18.1	66.5	16.6	Yes	Yes	Yes
PC (p-36:2)	53.4	15.2	61.8	17.2	60.4	16.7	Yes	Yes	No
PC (p-36:4)	53.6	17.7	64.2	18.2	60.0	18.6	Yes	Yes	No
PC (p-36:5)	40.4	15.8	55.2	16.9	47.7	16.9	Yes	Yes	Yes
PC (p-38:4)	47.5	18.6	61.6	22.8	58.5	21.2	Yes	Yes	No
PC (p-38:5)	45.5	14.3	58.8	16.9	52.3	15.4	Yes	Yes	Yes
PC (p-38:6)	52.0	15.0	65.0	18.0	59.6	16.8	Yes	Yes	Yes
PC (p-40:5)	48.8	14.1	68.2	18.7	58.2	16.6	Yes	Yes	Yes
PE (26:4)	38.2	13.0	45.4	14.9	40.6	14.0	Yes	No	Yes
PE (38:2)	44.0	20.3	48.6	22.5	50.5	22.8	Yes	Yes	No
PE (p-34:1)	47.4	15.8	51.7	17.2	55.2	19.0	Yes	Yes	No
PE (p-34:2)	44.2	20.6	55.9	22.6	54.8	25.1	Yes	Yes	No

PE (p-34:3)	51.5	12.0	52.9	12.1	50.7	12.0	No	No	No
PE (p-36:3)	52.8	12.0	66.7	16.3	58.9	13.9	Yes	Yes	Yes
PE (p-36:4)	56.1	16.2	67.4	17.3	64.7	19.4	Yes	Yes	No
PE (p-34:1)	45.2	21.6	30.6	17.8	40.5	21.4	Yes	Yes	Yes
PE (p-40:5)	58.1	18.1	39.5	15.2	48.0	18.9	Yes	Yes	Yes
SM (d18:1/17:0)	27.7	13.0	49.4	29.1	34.4	18.1	Yes	Yes	Yes
SM (d18:1/20:0)	56.5	18.3	54.4	18.4	61.8	20.3	No	Yes	Yes
SM (d18:1/21:1)	49.6	17.5	65.2	20.8	59.5	21.3	Yes	Yes	Yes
SM (d18:1/23:2)	58.9	13.9	69.7	15.0	67.1	16.3	Yes	Yes	No
SM (d18:1/24:0)	52.8	14.4	72.6	18.1	61.7	16.1	Yes	Yes	Yes
SM (d18:1/24:3)	44.9	13.9	66.1	21.8	53.6	16.9	Yes	Yes	Yes
CAR (16:0)	37.0	17.1	44.3	17.2	38.5	15.6	Yes	No	Yes
CAR (18:1)	21.6	4.8	24.0	3.6	22.4	4.2	Yes	No	Yes
2H Cer (d18:1/20:1)	42.1	20.4	33.6	9.6	36.2	14.3	Yes	Yes	No
2H Cer (d18:1/25:1)	57.6	16.0	48.6	14.8	52.3	15.8	Yes	Yes	Yes
2H OH Cer (d18:1/20:0)	46.0	13.7	50.4	14.7	48.2	15.1	Yes	No	No
Glc(d18:1/26:1 (17Z))	44.2	19.6	29.7	10.7	36.4	14.9	Yes	Yes	Yes

[a] t-test probabilities were calculated to determine if there are statistically significant differences in localizations of each detected ion among red pulp, white pulp, and marginal zone regions. ‘Yes’ in green indicates significant differences between the compared areas. ‘No’ in orange indicates no significant difference between the compared areas. Probabilities are significant at a 99% confidence interval.

Conclusions

We have developed and evaluated a new computational workflow to register LA-ICP-MS and MALDI-MS images. Our workflow is written in Python and contains functions for image pre-processing, dimensionality reduction, registration, and validation. It is freely available via GitHub at https://github.com/Vachet-Lab/MS-Registration. Registration of MALDI-MS and LA-ICP-MS images of adjacent tissue sections can be performed, enabling registrations of the two imaging modalities with accuracies within ± 50 μm. The computational workflow generates a unified dataset, enabling quantitative comparisons of tissues from mice treated with nanomaterial siRNA delivery systems. The resulting quantitative correlations provide insight into how the nanomaterials influence lipid levels in site-specific manner, which will allow us to more carefully study how nanomaterial delivery systems influence biochemistry in tissues. Additionally, registration of LA-ICP-MS and MALDI-MS images allows us to leverage the higher precision data associated with LA-ICP-MS imaging to better segment MALDI-MS images. The improved segmentation leads to identification of lipids that are most associated with each of the three different sub-organ regions of the spleen. We expect that in the future other statistical models, already present as libraries in Python or elsewhere, can be used to further deepen our understanding of drug delivery systems.

Acknowledgements

This research was supported by the National Science Foundation, Grant CHE-2108044. We thank Professor Vincent M. Rotello and researchers (Xianzhi Zhang, Roberto Cao-Milan, Yuanchang Liu, Yi-Wei Lee) in his lab at the University of Massachusetts Amherst for the nanoparticle samples.

Conflicts of Interest

There are no conflicts of interest to declare.

Author Contributions

L.J.C and R.W.V. conceptualized the study. L.J.C., K.N.S., and J.D. performed the experiments and analyzed the data. L.J.C. wrote the new software. L.J.C. and R.W.V wrote the manuscript.

References

1 A. R. Buchberger, K. DeLaney, J. Johnson and L. Li, *Anal. Chem.*, 2018, **90**, 240–265.

2 R. M. A. Heeren, *Int. J. Mass Spectrom.*, 2015, **377**, 672–680.

3 R. M. Caprioli, T. B. Farmer and J. Gile, *Anal. Chem.*, 1997, **69**, 4751–4760.

4 J. L. Norris and R. M. Caprioli, *Chem. Rev.*, 2013, **113**, 2309–2342.

5 M. M. Gessel, J. L. Norris and R. M. Caprioli, *J. Proteomics*, 2014, **107**, 71–82.

6 D. S. Cornett, M. L. Reyzer, P. Chaurand and R. M. Caprioli, *Nat. Methods.*, 2007, **4**, 828–833.

7 D. R. Ifa, J. M. Wiseman, Q. Song and R. G. Cooks, *Int. J. Mass Spectrom.*, 2007, **259**, 8–15.

8 K. Y. Garza, C. L. Feider, D. R. Klein, J. A. Rosenberg, J. S. Brodbelt and L. S. Eberlin, *Anal. Chem.*, 2018, **90**, 7785–7789.

9 Y.-N. Ho, L.-J. Shu and Y.-L. Yang, *Wiley Interdiscip. Rev. Syst. Biol. Med.*, 2017, **9**, e1387.

10 A. Kleinridders, H. A. Ferris, M. L. Reyzer, M. Rath, M. Soto, M. L. Manier, J. Spraggins, Z. Yang, R. C. Stanton, R. M. Caprioli and C. R. Kahn, *Mol. Metab.*, 2018, **12**, 113–121.

11 S. R. Ellis, M. R. L. Paine, G. B. Eijkel, J. K. Pauling, P. Husen, M. W. Jervelund, M. Hermansson,

C. S. Ejsing and R. M. A. Heeren, *Nat. Methods.*, 2018, **15**, 515–518.

12 D. Touboul, O. Laprévote and A. Brunelle, *Curr. Opin. Chem. Biol.*, 2011, **15**, 725–732.

13 K. Huber, P. Khamehgir-Silz, T. Schramm, V. Gorshkov, B. Spengler and A. Römpp, *Anal. Bioanal. Chem.*, 2018, **410**, 5825–5837.

14 E. Gemperline, C. Keller, D. Jayaraman, J. Maeda, M. R. Sussman, J.-M. Ané and L. Li, *J. Proteome Res.*, 2016, **15**, 4403–4411.

15 D. J. Ryan, J. M. Spraggins and R. M. Caprioli, *Curr. Opin. Chem. Biol.*, 2019, **48**, 64–72.

16 V. Llombart, S. A. Trejo, S. Bronsoms, A. Morancho, M. Feifei, J. Faura, T. García-Berrocoso, A. Simats, A. Rosell, F. Canals, M. Hernández-Guillamón and J. Montaner, *J. Proteomics.*, 2017, **152**, 243–253.

17 J. G. Swales, G. Hamm, M. R. Clench and R. J. A. Goodwin, *Int. J. Mass Spectrom.*, 2019, **437**, 99–112.

18 C. W. Chumbley, M. L. Reyzer, J. L. Allen, G. A. Marriner, L. E. Via, C. E. Barry and R. M. Caprioli, *Anal. Chem.*, 2016, **88**, 2392–2398.

19 M. R. Groseclose and S. Castellino, *Anal. Chem.*, 2013, **85**, 10099–10106.

20 D. Pozebon, G. L. Scheffler and V. L. Dressler, *J. Anal. At. Spectrom.*, 2017, **32**, 890–919.

21 A. Sussulini, J. S. Becker and J. S. Becker, *Mass Spectrom. Rev.*, 2017, **36**, 47–57.

22 J. Sabine Becker, *J. Mass Spectrom.*, 2013, **48**, 255–268.

23 N. H. Patterson, E. Yang, E. Kranjec and P. Chaurand, *Bioinformatics.*, 2019, **35**, 1261–1262.

24 E. K. Neumann, K. V. Djambazova, R. M. Caprioli and J. M. Spraggins, *J. Am. Soc. Mass Spectrom.*, 2020, **31**, 2401–2415.

25 J. E. Cassat, J. L. Moore, K. J. Wilson, Z. Stark, B. M. Prentice, R. Van de Plas, W. J. Perry, Y. Zhang, J. Virostko, D. C. Colvin, K. L. Rose, A. M. Judd, M. L. Reyzer, J. M. Spraggins, C. M. Grunenwald, J. C. Gore, R. M. Caprioli and E. P. Skaar, *Sci. Transl. Med.*, 2018, **10**, eaan6361.

26 W. J. Perry, J. M. Spraggins, J. R. Sheldon, C. M. Grunenwald, D. E. Heinrichs, J. E. Cassat, E. P. Skaar and R. M. Caprioli, *Proc. Natl. Acad. Sci.*, 2019, **116**, 21980–21982.

27 I. Kaya, S. Sämfors, M. Levin, J. Borén and J. S. Fletcher, *J. Am. Soc. Mass Spectrom.*, 2020, **31**, 2133–2142.

28 T. Porta Siegel, G. Hamm, J. Bunch, J. Cappell, J. S. Fletcher and K. Schwamborn, *Mol. Imaging Biol.*, 2018, **20**, 888–901.

29 S. A. Iakab, P. Ràfols, X. Correig-Blanchar and M. García-Altares, *Anal. Chem.*, 2021, **93**, 6301–6310.

30 E. K. Neumann, T. J. Comi, N. Spegazzini, J. W. Mitchell, S. S. Rubakhin, M. U. Gillette, R. Bhargava and J. V. Sweedler, *Anal. Chem.*, 2018, **90**, 11572–11580.

31 T. W. Bocklitz, A. C. Crecelius, C. Matthäus, N. Tarcea, F. Von Eggeling, M. Schmitt, U. S. Schubert and J. Popp, *Anal. Chem.*, 2013, **85**, 10829–10834.

32 F. Tobias and A. B. Hummon, *J. Proteome Res.*, 2020, **19**, 3620–3630.

33 K. N. Sikora, J. M. Hardie, L. J. Castellanos-García, Y. Liu, B. M. Reinhardt, M. E. Farkas, V. M. Rotello and R. W. Vachet, *Anal. Chem.*, 2020, **92**, 2011–2018.

34 A.-C. Niehoff, J. Schulz, J. Soltwisch, S. Meyer, H. Kettling, M. Sperling, A. Jeibmann, K. Dreisewerd, K. A. Francesconi, T. Schwerdtle and U. Karst, *Anal. Chem.*, 2016, **88**, 5258–5263.

35 R. González de Vega, M. L. Fernández Sanchez, N. Eiro, F. J. Vizoso, M. Sperling, U. Karst and A. Sanz Medel, *Anal. Bioanal. Chem.*, 2018, **410**, 913–922.

36 N. H. Patterson, M. Tuck, A. Lewis, A. Kaushansky, J. L. Norris, R. Van De Plas and R. M. Caprioli, *Anal. Chem.*, 2018, **90**, 12404–12413.

37 S. J. M. Van Malderen, B. Laforce, T. Van Acker, C. Nys, M. De Rijcke, R. De Rycke, M. De Bruyne, M. N. Boone, K. De Schamphelaere, O. Borovinskaya, B. De Samber, L. Vincze and F. Vanhaecke, *Anal. Chem.*, 2017, **89**, 4161–4168.

38 M. Holzlechner, M. Bonta, H. Lohninger, A. Limbeck and M. Marchetti-Deschmann, *Anal. Chem.*, 2018, **90**, 8831–8837.

39 H. Lohninger and J. Ofner, *Spectrosc. Eur.*, 2014, **26**, 6–10.

40 M. Brust, M. Walker, D. Bethell, D. J. Schiffrin and R. Whyman, *J. Chem. Soc., Chem. Commun.*, 1994, **7**, 801–802.

41 A. Chompoosor, G. Han and V. M. Rotello, *Bioconjug. Chem.*, 2008, **19**, 1342–1345.

42 S. T. Kim, K. Saha, C. Kim and V. M. Rotello, *Acc. Chem. Res.*, 2013, **46**, 681–691.

43 Y. Jiang, S. Huo, T. Mizuhara, R. Das, Y. W. Lee, S. Hou, D. F. Moyano, B. Duncan, X. J. Liang and V. M. Rotello, *ACS Nano*, 2015, **9**, 9986–9993.

44 B. Yan, Z.-J. Zhu, O. R. Miranda, A. Chompoosor, V. M. Rotello and R. W. Vachet, *Anal. Bioanal. Chem.*, 2010, **396**, 1025–1035.

45 Y. Jiang, R. Tang, B. Duncan, Z. Jiang, B. Yan, R. Mout and V. M. Rotello, *Angew. Chemie Int. Ed.*, 2014, **54**, 506–510.

46 J. Hardie, Y. Jiang, E. R. Tetrault, P. C. Ghazi, G. Y. Tonga, M. E. Farkas and V. M. Rotello, *Nanotechnology.*, 2016, **27**, 374001.

47 Y. Jiang, J. Hardie, Y. Liu, M. Ray, X. Luo, R. Das, R. F. Landis, M. E. Farkas and V. M. Rotello, *J. Control. Release.*, 2018, **283**, 235–240.

48 P. Chaurand, D. S. Cornett, P. M. Angel and R. M. Caprioli, *Mol. Cell. Proteomics.*, 2011, **10**, S1–S11.

49 S. G. Elci, B. Yan, S. T. Kim, K. Saha, Y. Jiang, G. A. Klemmer, D. F. Moyano, G. Y. Tonga, V. M. Rotello and R. W. Vachet, *Analyst*, 2016, **141**, 2418–2425.

50 S. G. Elci, Y. Jiang, B. Yan, S. T. Kim, K. Saha, D. F. Moyano, G. Yesilbag Tonga, L. C. Jackson, V. M. Rotello and R. W. Vachet, *ACS Nano*, 2016, **10**, 5536–5542.

51 S. G. Elci, G. Y. Tonga, B. Yan, S. T. Kim, C. S. Kim, Y. Jiang, K. Saha, D. F. Moyano, A. L. M. Marsico, V. M. Rotello and R. W. Vachet, *ACS Nano.*, 2017, **11**, 7424–7430.

52 D. Fay, A. D. Palmer, K. Vitaly and T. Alexandrov, pyimzML.,

https://github.com/alexandrovteam/pyimzML, (accessed 11 January 2020).

53 L. J. Castellanos-García, S. Gokhan Elci and R. W. Vachet, *Analyst*, 2020, **145**, 3705–3712.

54 K. Ovchinnikova, L. Stuart, A. Rakhlin, S. Nikolenko and T. Alexandrov, *Bioinformatics*, 2020, **36**, 3215–3224.

55 F. Pedregosa, G. Varoquaux, A. Gramfort, V. Michael, B. Thirion, O. Grisel, M. Blondel, P. Prettenhofer, R. Weiss, V. Dubourg, J. Vanderplas, A. Passos, D. Cournapeau, M. Brucher, M. Perrot and E. Duchesnay, *J. Mach. Learn. Res.*, 2011, **12**, 2825–2830.

56 B. Lowekamp, K. Marstal, D. Blezek, D. Chen, Z. Yaniv and B. King, *GitHub*, 2020.

57 S. Klein, M. Staring, K. Murphy, M. A. Viergever and J. P. W. Pluim, *IEEE Trans. Med. Imaging.*, 2010, **29**, 196–205.

58 J. Schindelin, I. Arganda-Carreras, E. Frise, V. Kaynig, M. Longair, T. Pietzsch, S. Preibisch, C. Rueden, S. Saalfeld, B. Schmid, J. Y. Tinevez, D. J. White, V. Hartenstein, K. Eliceiri, P. Tomancak and A. Cardona, *Nat. Methods.*, 2012, **9**, 676–682.

59 P. Virtanen, R. Gommers, T. E. Oliphant, M. Haberland, T. Reddy, D. Cournapeau, E. Burovski, P. Peterson, W. Weckesser, J. Bright, S. J. Van Der Walt, M. Brett, J. Wilson, K. J. Millman, N. Mayorov, A. R. J. Nelson, E. Jones, R. Kern, E. Larson, C. J. Carey, I. Polat, Y. Feng, E. W. Moore, J. VanderPlas, D. Laxalde, J. Perktold, R. Cimrman, I. Henriksen, E. A. Quintero, C. R. Harris, A. M. Archibald, A. H. Ribeiro, F. Pedregosa and P. van Mulbregt, *Nat. Methods.*, 2020, **17**, 261–272.

60 W. M. Abdelmoula, K. Škrášková, B. Balluff, R. J. Carreira, E. A. Tolner, B. P. F. Lelieveldt, L. van der Maaten, H. Morreau, A. M. J. M. van den Maagdenberg, R. M. A. Heeren, L. A. McDonnell and J. Dijkstra, *Anal. Chem.*, 2014, **86**, 9204–9211.

61 W. M. Abdelmoula, B. Balluff, S. Englert, J. Dijkstra, M. J. T. Reinders, A. Walch, L. A. McDonnell and B. P. F. Lelieveldt, *Proc. Natl. Acad. Sci. U. S. A.*, 2016, **113**, 12244–12249.

62 W. Gardner, S. M. Cutts, D. R. Phillips and P. J. Pigram, *Biopolymers.*, 2021, **112**, e23400.

63 T. Rohlfing, *IEEE Trans. Med. Imaging.*, 2012, **31**, 153–163.

64 M. A. Jones, S. H. Cho, N. H. Patterson, R. Van de Plas, J. M. Spraggins, M. R. Boothby and R. M. Caprioli, *Anal. Chem.*, 2020, **92**, 7079–7086.

65 C. Zhao, T. Yong, Y. Zhang, Y. Jin, Y. Xiao, H. Wang, B. Zhao and Z. Cai, *Environ. Int.*, 2020, **135**, 105378.

66 M. Wallace, C. Morris, C. M. O'Grada, M. Ryan, E. T. Dillon, E. Coleman, E. R. Gibney, M. J. Gibney, H. M. Roche and L. Brennan, *Mol. Biosyst.*, 2014, **10**, 1586–1595.

67 W. Khovidhunkit, M. S. Kim, R. A. Memon, J. K. Shigenaga, A. H. Moser, K. R. Feingold and C. Grunfeld, *J. Lipid Res.*, 2004, **45**, 1169–1196.

68 N. Parameswaran and S. Patial, *Crit Rev Eukaryot Gene Expr.*, 2010, **20**, 87–103.

69 A. M. Oros-Peusquens, A. Matusch, J. S. Becker and N. J. Shah, *Int. J. Mass Spectrom.*, 2011, **307**, 245–252.

70 T. Alexandrov and J. H. Kobarg, *Bioinformatics.*, 2011, **27**, i230–i238.

71 T. Alexandrov, M. Becker, S.-O. Deininger, G. Ernst, L. Wehder, M. Grasmair, F. von Eggeling, H. Thiele and P. Maass, *J. Proteome Res.*, 2010, **9**, 6535–6546.

72 K. D. Bemis, A. Harry, L. S. Eberlin, C. R. Ferreira, S. M. van de Ven, P. Mallick, M. Stolowitz and O. Vitek, *Mol. Cell. Proteomics.*, 2016, **15**, 1761–1772.

73 R. E. Mebius and G. Kraal, *Nat. Rev. Immunol.*, 2005, **5**, 606–616.